ORNL/TM-2019/2117
CRADA/NFE-17-06604

Comparison of Electron Beam and Laser Beam Powder Bed Fusion Additive Manufacturing Process for High Temperature Turbine Component Materials, Phase II

CRADA FINAL REPORT
NFE-17-06604

Sebastien Dryepondt
Daniel Ryan
Mike Kirka

June 30, 2019

Approved for Public Release.
Distribution is Unlimited.

OAK RIDGE NATIONAL LABORATORY
MANAGED BY UT-BATTELLE FOR THE US DEPARTMENT OF ENERGY

ORNL/TM-2019/2117
CRADA/NFE- 17-06604

Materials Science and Technology Division
Advanced Manufacturing Office

Comparison of Electron Beam and Laser Beam Powder Bed Fusion Additive Manufacturing Process for High Temperature Turbine Component Materials, Phase II

Authors
Sebastien Dryepondt
Michael Kirka
Daniel Ryan

Date Published:
June 28, 2019

Prepared by
OAK RIDGE NATIONAL LABORATORY
Oak Ridge, Tennessee 37831-6283
managed by
UT-BATTELLE, LLC
for the
US DEPARTMENT OF ENERGY
under contract DE-AC05-00OR22725

CONTENTS

LIST OF FIGURES

ACKNOWLEDGEMENTS

This CRADA NFE-17-06604 was conducted as a Technical Collaboration project within the Oak Ridge National Laboratory (ORNL) Manufacturing Demonstration Facility (MDF) sponsored by the US Department of Energy Advanced Manufacturing Office (CPS Agreement Number 24761). Opportunities for MDF technical collaborations are listed in the announcement "Manufacturing Demonstration Facility Technology Collaborations for US Manufacturers in Advanced Manufacturing and Materials Technologies" posted at http://web.ornl.gov/sci/manufacturing/docs/FBO-ORNL-MDF-2013-2.pdf. The goal of technical collaborations is to engage industry partners to participate in short-term, collaborative projects within the Manufacturing Demonstration Facility (MDF) to assess applicability and of new energy efficient manufacturing technologies. Research sponsored by the U.S. Department of Energy, Office of Energy Efficiency and Renewable Energy, Advanced Manufacturing Office, under contract DE-AC05-00OR22725 with UT-Battelle, LLC.

The authors would like to thank T. Jordan, C. Stevens, C.S. Hawkins, T. Evans, C. Briseño, and L. McNeilly for their help with experimental work and P. Fernandez-Zelaia and M. Romedenne for reviewing the manuscript.

ABSTRACT

The evolving additive manufacturing (AM) technology is now at the point where some metallic turbine components are being fabricated for both development and production purposes. The goal of this phase II project is to continue the evaluation of AM Nickel Alloy X fabricated by electron beam (EB) or laser beam (LB) powder bed fusion (PBF) process for gas turbine applications. Microstructure, mechanical and oxidation properties characterization was conducted on test specimens produced with powders of different chemistries within the typical material specification range. Powders with high Silicon (Si) content for the LB-PBF and low Si content for the EB-PBF displayed significant cracking levels in the AM Nickel Alloy X material. Accordingly, optimum fatigue performance would require careful control of powder chemistry, optimization of the fabrication parameters for a given powder and use of hot isostatic pressing (HIP) post treatment. Oxidation testing conducted at 1472°F (800ºC) in air showed that the roughness of the EB-PBF specimens led to an increase in specimen mass change, but overall the AM specimens exhibited oxidation behavior at 1472°F (800ºC) that is appropriate for applications in gas turbine engines. Assessment of the geometric capability of the LB-PBF and EB-PBF systems using artifacts representative of turbine component geometries revealed that the LB-PBF process is well-suited for the fabrication of intricate geometries needed for turbine engine fuel injector components, but further process development is required to improve the EB-PBF system feature resolution.

1. COMPARISON OF ELECTRON BEAM AND LASER BEAM POWDER BED FUSION ADDITIVE MANUFACTURING PROCESS FOR HIGH TEMPERATURE TURBINE COMPONENT MATERIALS

This phase II technical collaboration project (NFE-17-06604) was begun on April 19, 2017 and was completed on June 30, 2019. The collaboration partner Solar Turbines Incorporated is a large business which is a wholly owned subsidiary of Caterpillar Inc. The mechanical properties of AM Nickel Alloy X specimens fabricated by EB-PBF and LB-PBF processes met the specification requirements for cast Nickel Alloy X, but the alloy chemistry must be controlled to avoid crack formation during AM fabrication.

1.1 BACKGROUND

Solar Turbines has over 50 years of experience with the design, development and commercialization of industrial gas turbines and turbomachinery products. Solar Turbines has an established record of development of gas turbine technologies from internally funded and government programs. An example of a successful government-industry partnership was the DOE-Solar Advanced Turbine Systems (ATS) program, which resulted in the development of the 4.6 MWe Mercury 50 recuperated gas turbine.

More recently, collaborative work by Solar Turbines and ORNL under CRADA NFE-15-05495 in phase I of the project revealed the Electron Beam Powder Bed Fusion (EB-PBF) and Laser Beam Powder Bed Fusion (LB-PBF) materials properties displayed substantial overlap with those of conventional cast and wrought forms of Nickel Alloy X materials currently used in gas turbine applications, indicative that the subject AM materials are viable alternatives for manufacture of some turbine components [1]. However, this initial assessment of EB and LB AM materials also revealed significant differences in tensile, creep and fatigue resistance. Another important finding from EB-PBF work conducted at ORNL was the impact of slight changes of Silicon (Si) content on EB-PBF Nickel Alloy X microstructure. Si is also known to play a role in the formation of hot tearing cracks during

LB-PBF [2].

The goal of the phase II project was to support the use of AM for rapidly redesigning and qualifying Nickel Alloy X components to improve gas turbine performance and durability. In order to produce actual components within tight dimension tolerances, knowledge of the AM processes geometric capability must be gained. Task 1 of this phase II project focused on the fabrication by EB and LB-PBF of artifacts representative of geometric features in industrial gas turbine engine components.

Certification of multiple powder sources reduces the risk of unanticipated interruption of precursor material supply. Ensuring continuous and stable powder procurement is essential for cost effective AM part production. In Task 2, the effect of powders from different providers and of different Mn and Si contents on the AM Nickel Alloy X mechanical properties were assessed.

Finally, the goal of Task 3 was to continue the AM Nickel Alloy X material properties characterization initiated in phase I. Generation of a more comprehensive set of data was needed for component design analysis activities. Mechanical testing horizontal and perpendicular to the build direction was therefore conducted on AM Nickel Alloy X, and the AM Nickel Alloy X high temperature oxidation resistance was assessed at 1472°F (800ºC) in air.

1.2 TECHNICAL RESULTS

1.2.1 Specimen Fabrication

Powder Characterization: Solar Turbines purchased from different powder producers EB-PBF and LB-PBF Nickel Alloy X powders with either a “high” or “low” Si content. The resulting powder chemistries are given in Table 1. In addition to a very low Si content, very low Mn and C contents were measured for the low Si EB- and LB-PBF powders, with also relatively high Al and Ti contents. The high Si powder chemistry was close to the chemistry of the powders used for the project’s phase I.

The particle size distribution (PSD) was measured using commercially available laser diffraction equipment and physical sieves. The results are summarized in Table 2. The PSD for both the EB-PBF and LB-PBF processes were consistent with the targeted PSD, with a slight variation for the LB-PBF process between the low and high Si powders. The scanning electron microscopy (SEM) micrographs shown in Figure 1 revealed for all type of powders the occurrence of satellites on spherical particles, with also a few irregularly shaped particles.

AM Machines: A Concept Laser M2 machine was used for the LB-PBF fabrication at Solar Turbines, while an Arcam S12 machine was used at ORNL for the EB-PBF specimens and artifacts (Figure 2). It is worth noting that a LB-PBF 3D Systems ProX300 machine was used for the phase I of the project, so new M2 specific fabrication parameters were used for phase II. For the EB-PBF process, the fabrication parameters optimized during the phase I were used for all the builds fabricated during phase II.

Test Bars and Artifacts: Examples of the test bars and plates fabricated by LB-PBF and EB-PBF using the high Si and low Si powders are shown in Figure 3. To conduct mechanical testing perpendicular to the build direction, horizontal LB-PBF bars were produced while large rectangular plates were fabricated by EB-PBF.

Hollow cube and vane artifacts representative of features in gas turbine components were also fabricated to assess the geometry capability of the LB-PBF and EB-PBF machines. In addition, thin walled specimens, 1 to 1.5mm thick, were fabricated for oxidation testing. An example of the artifacts and thin wall build configuration for the LB-PBF machine is displayed in Figure 4.

Heat Treatment: Two types of post heat treatments were conducted on the LB-PBF bars fabricated for mechanical testing: (1) 1 hour anneal at 2150ºF and (2) hot isostatic pressing (HIP) at 2125ºF for 3 hours with an applied stress of 15ksi. For the EB-PBF specimens, both the high Si and low Si alloys were tested in the as fabricated conditions, with the high Si alloys also being tested after HIP’ing at 2125ºF, 15ksi for 3 hours.

Table 1. Chemical composition (weight percent) of Low Si and High Si variants of Nickel Alloy X powders used for Laser and Electron Beam powder bed fusion additive manufacture of test articles

	LB-PBF (Low Si) Phase II	EB-PBF (Low Si) Phase II	LB-PBF (High Si) Phase II	EB-PBF (High Si) Phase II	LB-PBF (High Si) Phase I	EB-PBF (High Si) Phase I	AMS5390 (Min.)	AMS5390 (Max.)
Ni	Bal.	Bal.	Bal.	Bal.	Bal.	Bal.	Bal.	Bal.
Cr	20.51	20.6	20.73	21	21.5	21.7	20.5	23
Fe	18.31	18.5	17.93	19.4	19.0	18.7	17	20
Mo	8.98	9	9.03	8.9	9.1	9	8	10
Co	2.18	2	1.25	1	1.5	1.6	0.5	2.5
W	0.82	0.8	0.53	0.3	0.59	0.66	0.2	1
Si	0.11	0	0.82	0.9	0.84	0.86	--	1
Mn	0.01	0	0.75	0.9	0.84	0.93	--	1
Al	0.31	0.3	0.04	0.02	--	--	--	--
Ti	0.13	0.13	0.01	<0.01	--	--	--	--
C	0.01	0.02	0.05	0.1	0.08	0.06	--	0.1

Table 2: Nominal limits of minimum and maximum particle size of Low Si and High Si variants of Nickel Alloy X powders used for Laser and Electron Beam powder bed fusion additive manufacture of test articles

	PSD
LB-PBF (Low Si)	15-45 µm
EB-PBF (Low Si)	38-106 µm
LB-PBF (High Si)	5-38 µm
EB-PBF (High Si)	38-106 µm

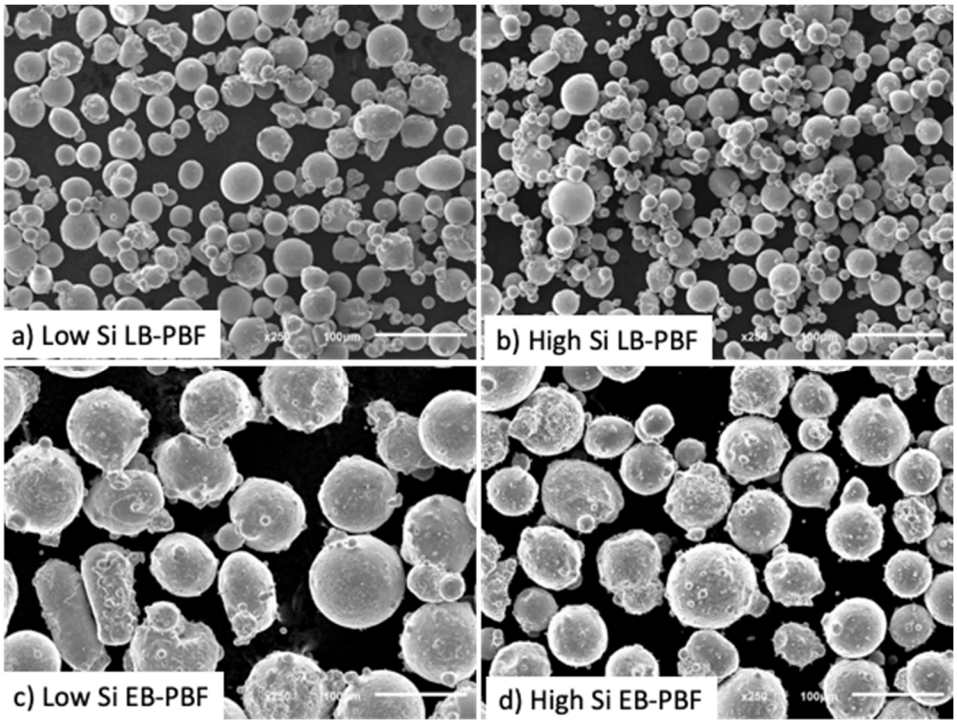

Figure 1: SEM images of metal powders showing nominally spherical particles with the regular occurrence of satellites and irregularly shaped particles, a) low Si, LB-PBF, b) high Si, LB-PBF, c) low Si, EB-PBF, d) high Si, EB-PBF

Figure 2: a) LB-PBF Concept Laser M2 machine, b) EB-PBF Arcam S12 machine

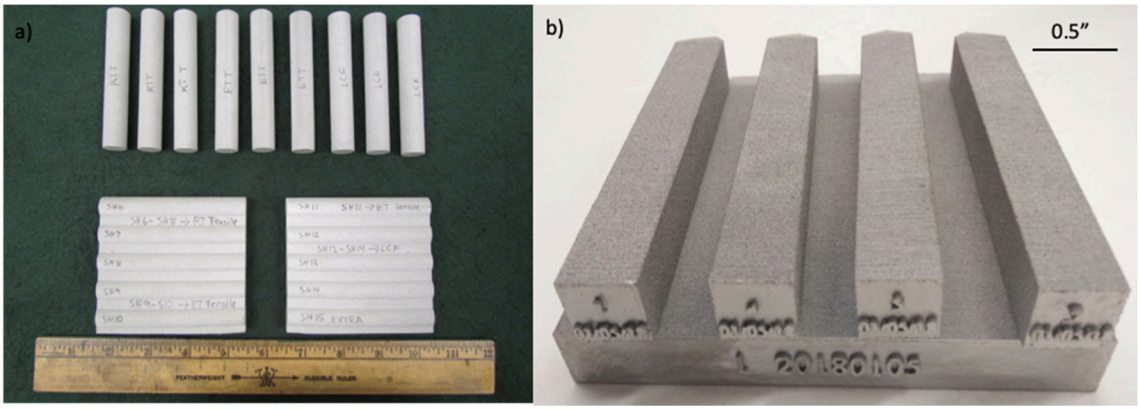

Figure 3: Mechanical test bar builds: a) LB-PBF Vertical and horizontal test bars, b) EB-PBF vertical bars and large plates to machine specimens perpendicular to the build direction

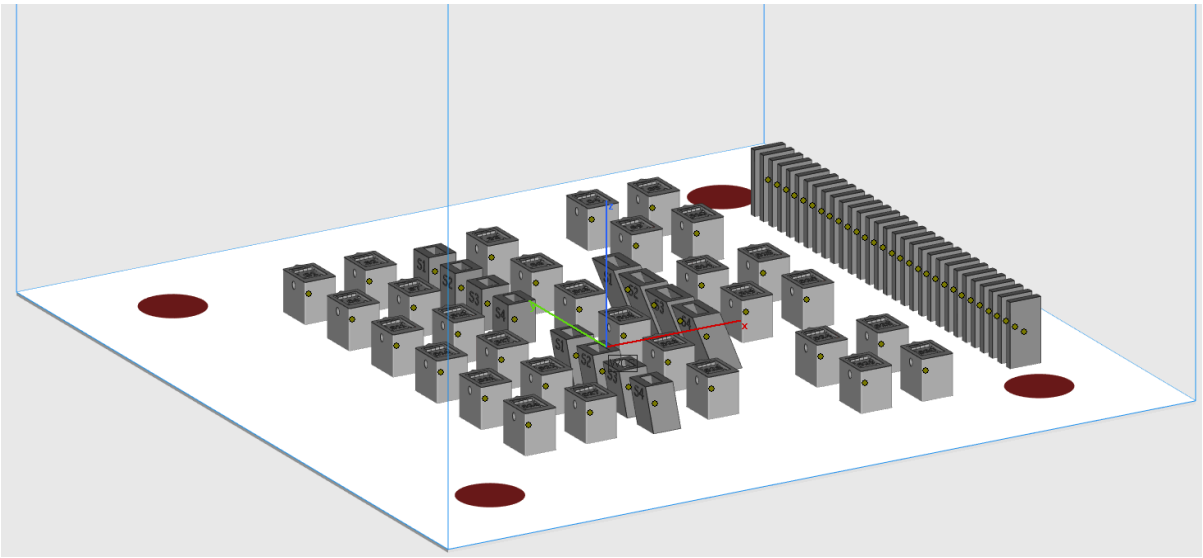

Figure 4: LB-PBF build plate layout for geometry (cube, vane), microstructural (cubes), and oxidation testing (panels)

1.2.2 AM Geometric Capability

AM Artifact Overview: Examples of the artifacts fabricated by EB- and LB-PBF processes are shown in Figure 5. Four different artifacts representative of gas turbine component features were built using both the high Si and low Si powders: one hollow cube with representative holes and thin walls of various thicknesses, and 0º, 20° and 45º vane artifacts. No significant differences were noticed between the high Si and low Si artifacts fabricated by LB-PBF. No characterization of the low Si EB-PBF artifacts was conducted due to the presence of large cracks in the alloy, as will be discussed later. The macroscopic top views of the cube artifacts presented in Figure 6 highlight the much better resolution achievable via LB-PBF compared to EB-PBF. For example, a step-function decrease of the thin wall thickness can be observed for the LB-PBF cube, as expected from the CAD drawing, while a uniform thickness is observed for the EB-PBF cube. The shape of the 4 holes is also more accurate for the LB-PBF artifact.

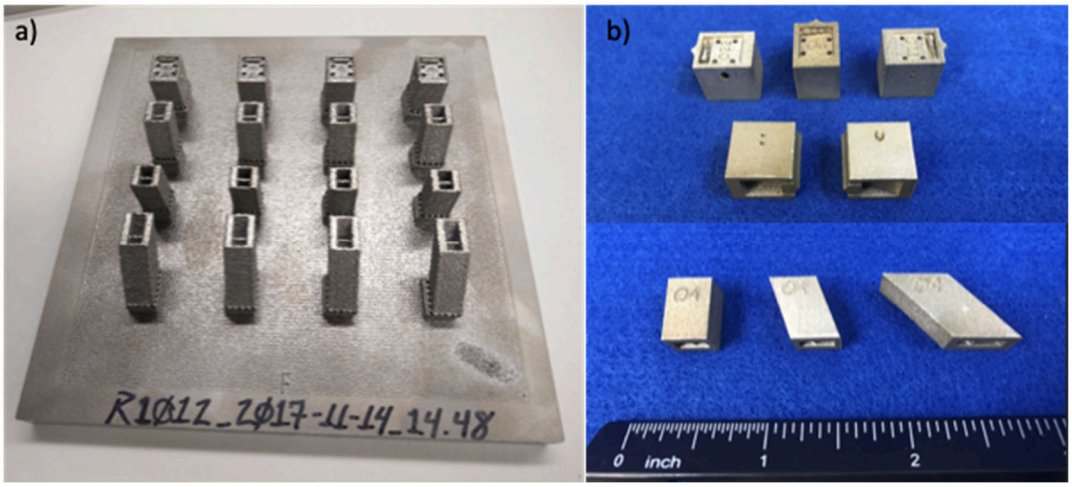

Figure 5: Artifact fabrication: a) Example of an artifact EB-PBF build, b) Top view of the 4 types of artifacts fabricated by LB-PBF: hollow cube with features, 0º vane, 20º vane and 45º vane artifacts

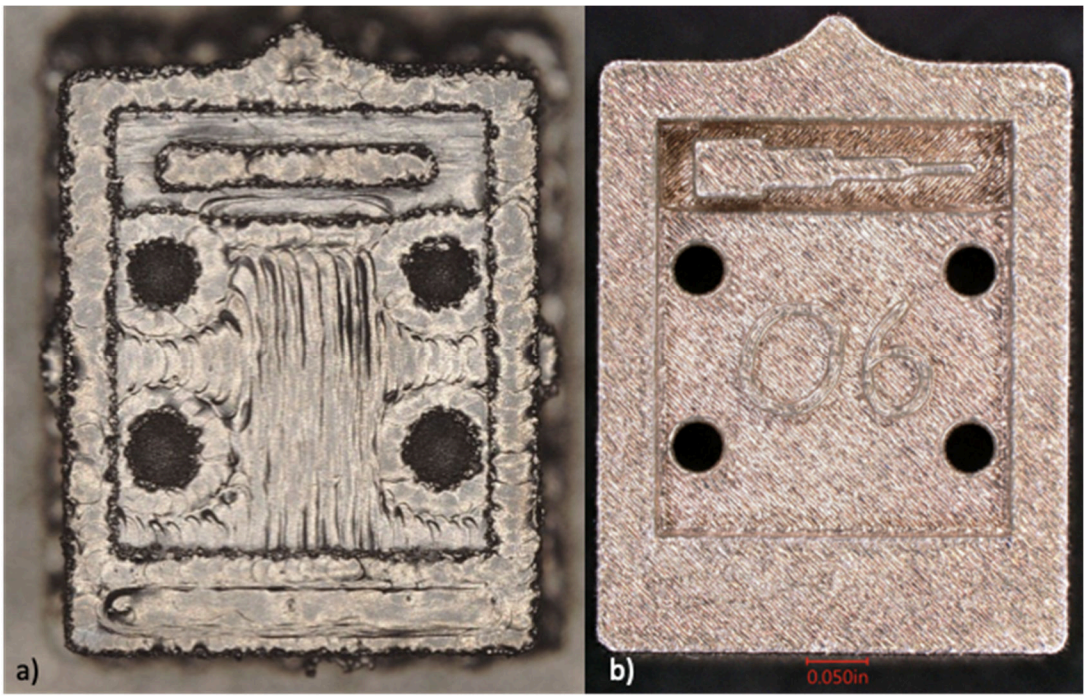

Figure 6: Comparison of the macroscopic top view for the cube artifacts, a) EB-PBF and b) LB-PBF showing the relative differences in geometric and surface finish capability between the two processes.

AM Artifact Surface Roughness: One of the main goals of the vane artifact fabrication was to assess the geometry capability of the EB-PBF and LB-PBF machines for angled thin walls. Measurement of the wall roughness was therefore conducted by image analysis on cross-section micrographs such as the one presented in Figure 7a-f. Images were imported in Python to determine the Rq values for the top and bottom walls, and the results are summarized in Figure 7g.

The roughness values from the LB-PBF vane artifacts were much lower than the roughness values calculated for the EB-PBF vane artifacts except for the bottom wall of the 45º LB-PBF vane

artifact. This is mainly due to the presence of a few large defects highlighted by white arrows in Figure 7c. It is also worth noting that the center walls of the EB-PBF vane artifacts are surrounded by unmelted powder particles trapped inside the artifacts. For EB-PBF component fabrication a procedure to remove the trapped particles would have to be incorporated.

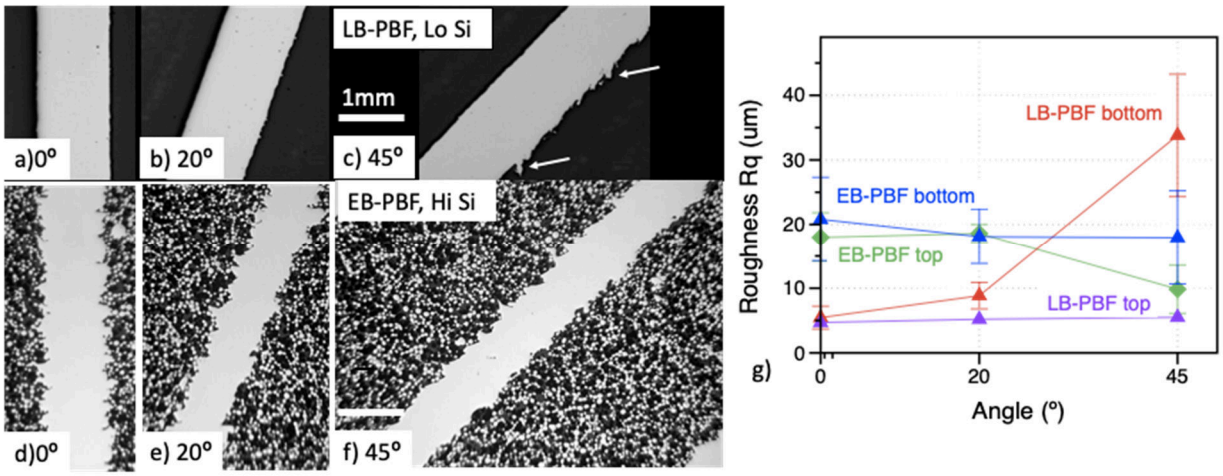

Figure 7: a-f) Cross-section optical micrographs of the vane artifacts, a) 0º LB-PBF, b) 20º LB-PBF, c) 45º LB-PBF, d) 0º EB-PBF, e) 20º EB-PBF, f) 45º LB-PBF, g) Rq values versus vane angle.

1.2.3 Microstructure Characterization (Precursor Powder Effect)

LB-PBF Microstructure: Microstructure characterization of the LB-PBF in the "as printed" condition (e.g. no heat treatment) revealed an overlapping hatched pattern typical of the LB-PBF process (Figure 8). The effect of powder composition on micro-cracking is shown in Figure 9. The low Si LB-PBF alloy was resistant to micro-cracks, but the high Si LB-PBF alloy displayed micro-cracking, with many of the cracks preferentially oriented along the build direction (i.e. vertical orientation).

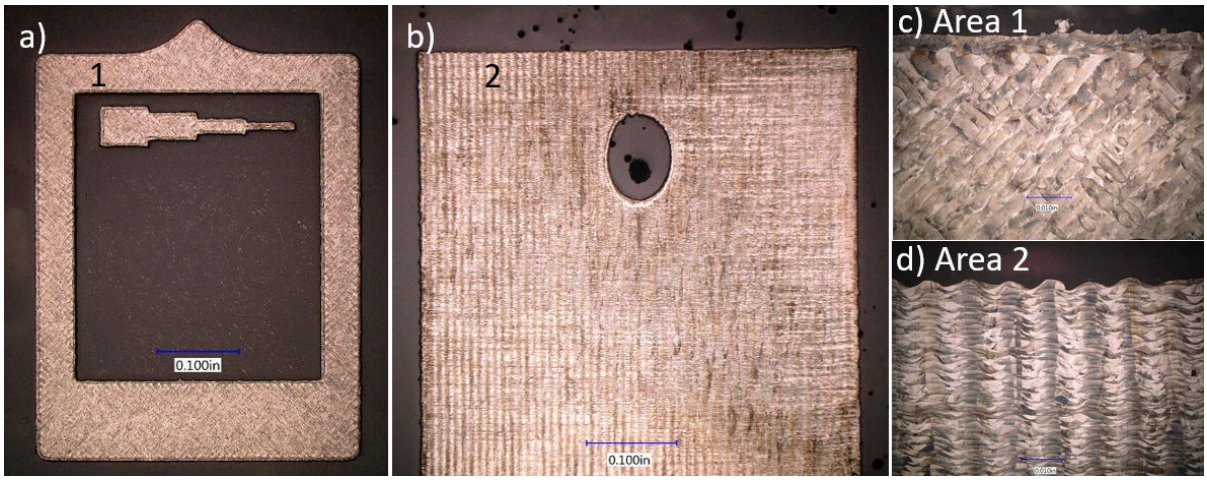

Figure 8: Optical micrograph of a representative LB-PBF cube sample in the as-printed heat treat condition showing typical microstructure of overlapping hatch patterns in the X-Y plane (a,c) and micro-weld profiles the Y-Z plane (b, d)

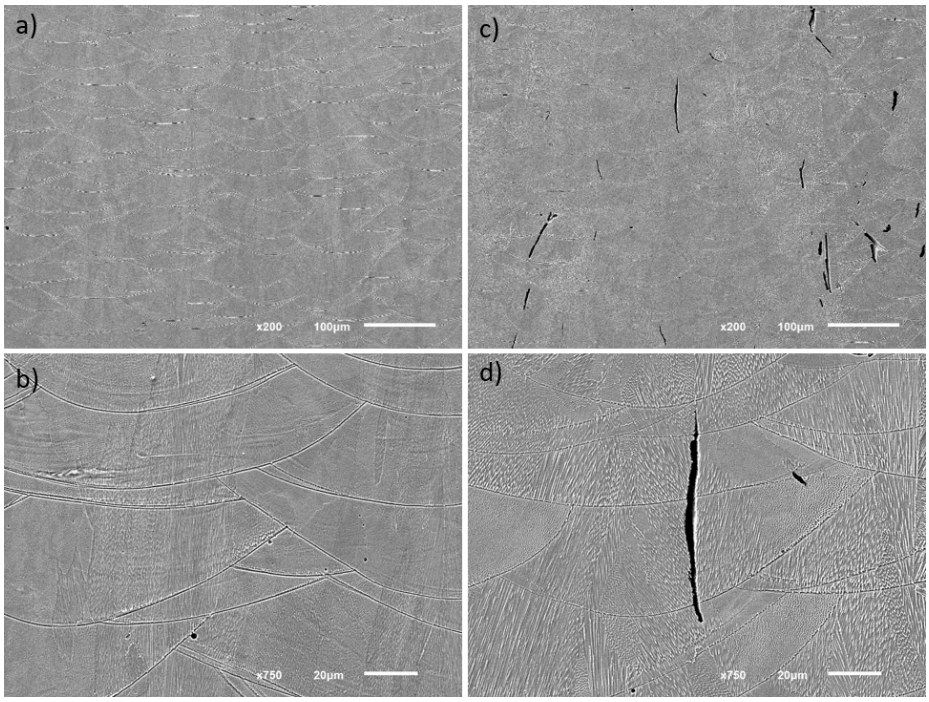

Figure 9: SEM images of the LB-PBF microstructure in the Y-Z plane illustrating the effect of chemistry on LB-PBF alloy micro-cracking, Low Si (a, b) was resistant to cracking, High Si (c, d) displayed micro-cracks mostly oriented in the build direction (Z axis).

EB-PBF Microstructure: Microstructure characterization of the EB-PBF low Si alloy was conducted on vertical test bars and representative microstructures are shown in Figure 10. Contrary to what was observed with LB-PBF, the alloy with decreased Si content exhibited very long hot-tear cracks located at grain boundaries. In addition, no precipitates were observed inside the grains or at grain boundaries. This might be an indication that the cooling rate after fabrication was relatively high and could have played a role in crack formation. Figure 10-d highlights the significant impact of these cracks on the tensile fracture mechanisms when tested perpendicular to the build direction. Due to the abundance of defects in the microstructure of the low Si EB-PBF alloy, it was decided to focus on the high Si EB-PBF alloy for the microstructure characterization and mechanical testing tasks.

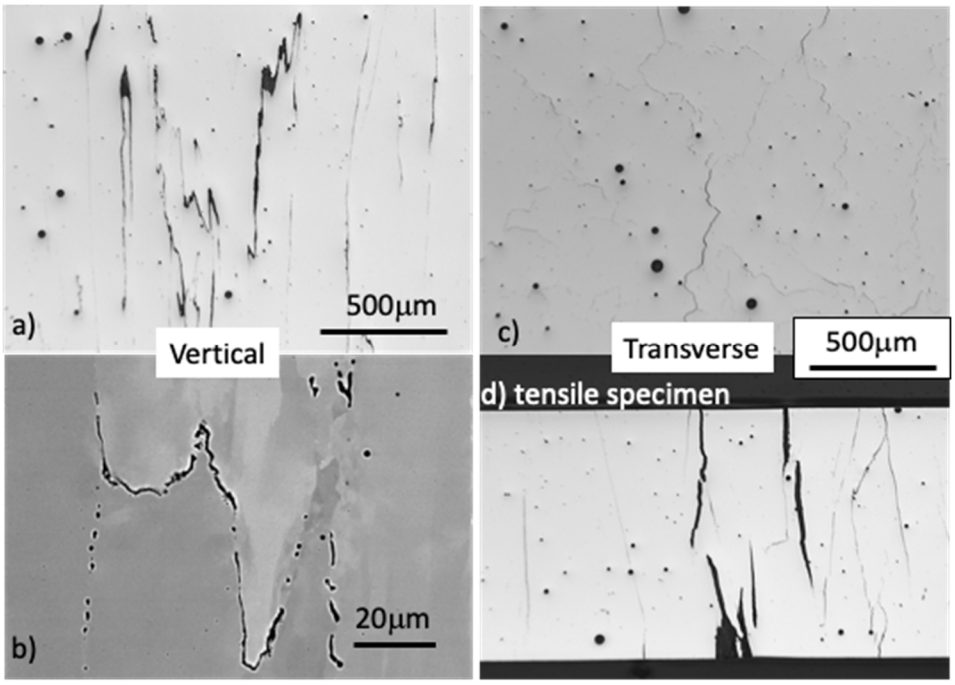

Figure 10: Cross-section micrographs of the Low Si EB-PBF alloy showing the presence of large cracks, a) optical micrographs of Y-Z plane (vertical orientation), b) SEM micrograph of Y-Z plane, c) Optical micrograph of X-Y plane (horizontal orientation), d) optical micrograph of a ruptured tensile specimen machined perpendicular to the build direction and tested at room temperature

Cross-section of two different cube artifacts, one polished from the top (X-Y plane) and the other one from the side (Y-Z plane), are shown in Figure 11. Red arrows highlight the presence of cracks (Figure 11b), typically observed close to the holes or in-between two holes. The location of these cracks is likely due to the specific artifact geometry. The SEM pictures shown in Figure 11d and 11e show elongated grains along the build direction with the presence of small cracks at some grain boundaries. A quite homogeneous dispersion of (Mo,Si)-rich precipitates were observed both in the grains and at grain boundaries. It is worth noting that cracking was not observed with the high Si EB-PBF material fabricated in phase I, and it was decided to process the phase II high Si EB-PBF material through the HIP treatment decribed previously (3h 2125ºF/14.75Ksi) before mechanical testing. Another difference between the two high Si EB-PBF materials is the preferential formation of continuous (Mo,Si) precipitates at grain boundaries in the Phase I alloy. The microstructure of the High Si EB-PBF alloy after HIP'ing is shown in Figure 12. The HIP treatment succesfully removed all the cracks and only micron-size voids were still present. HIP'ing did not impact the grain structure, but comparison between Figure 11e and Figure 12b highlights that a significant coarsening of the (Mo,Si) precipitates took place during HIP'ing.

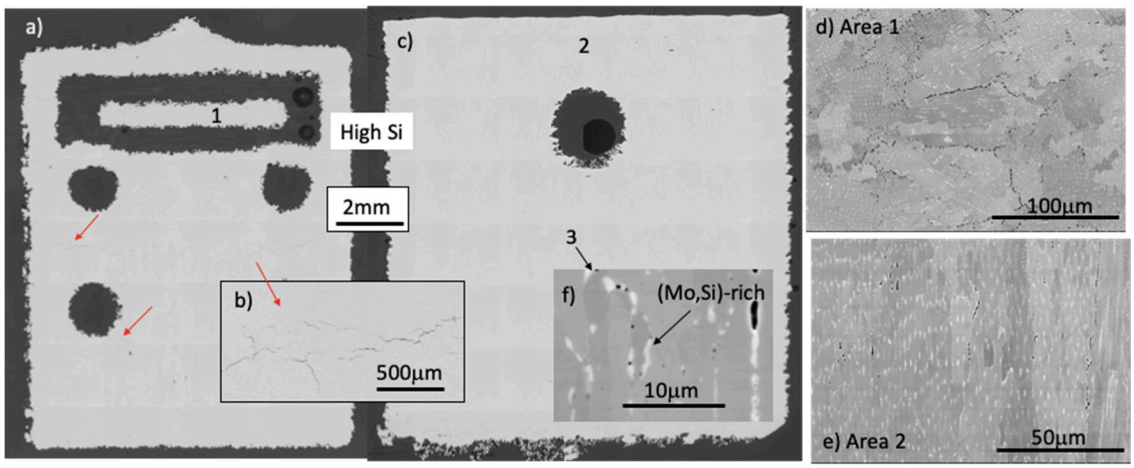

Figure 11: Cross-section micrographs of EB-PBF artifacts, a) General top view optical pictures of a cube artifact, b) Higher magnification optical pictures showing cracks, c) General side view of a cube artifact, d) SEM pictures of cube artifact showing defects at grain boundaries, e) SEM pictures of a cube artifact highlighting elongated grains along the build direction, f) High magnification SEM pictures showing the presence of (Mo,Si)-rich precipitates at grain boundaries

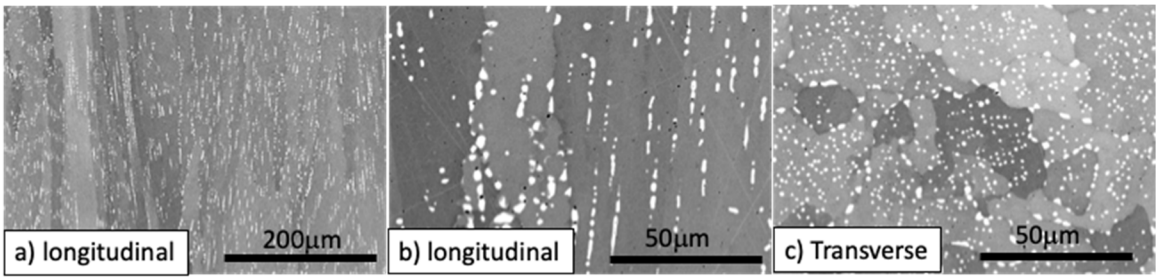

Figure 12: Effect of HIP'ing on the EB-PBF High Si material microstructure, a) and b) Longitudinal direction, c) Transverse direction

1.2.4 Mechanical Properties (Precursor Powder & Build Orientation Effect)

Tensile Properties: Figure 13 compares the tensile properties along the build direction of the annealed LB-PBF and as-fabricated EB-PBF alloys with a high Si or low Si content. Data from the high Si LB-PBF and EB-PBF alloys produced during phase I were added as well as average data for wrought Hastelloy X provided by Haynes International [1,3]. The LB-PBF high Si and low Si Nickel Alloy X alloys exhibited similar 0.2% yield (YS) and ultimate (UTS) tensile strength at room temperature and 1500ºF, but the ductility of the LB-PBF low Si was superior at room temperature. These tensile data were close to the tensile data for wrought Hastelloy X. The strength of both alloys was lower compared to the high Si phase I alloy, but the ductility was much higher. It is worth noting that two different LB-PBF machines were used for phase I and phase II and the annealing time was shorter for phase I (15 minutes) compared to phase II (1 hour).

The high Si phase II EB-PBF alloys showed superior YS and UTS compared to the phase I alloy, with UTS values similar to the UTS values measured for the LB-PBF phase II alloys. The alloy ductility was, however, quite low. A very brittle behavior was observed for the low Si EB-LBF alloy with low YS, UTS and ductility due to the presence of the large cracks.

As can be seen in Figure 14, HIP'ing had no effect on the tensile properties of the low Si LB-PBF alloy at room temperature and led to a slight increase of the alloy ductility at 1500ºF. For the high

Si LB-PBF alloy, limited decreases of the YS and UTS at room and 1500ºF were observed after HIP'ing, and a slight improvement of the ductility was observed at room temperature. Figure 14 also compares the properties of the LB-PBF alloys after annealing along and perpendicular to the build direction. For both the high Si and low Si LB-PBF alloys, the YS and UTS at room and 1500ºF were similar or slightly higher perpendicular to the build direction. A significant decrease of the ductility for the specimens machined from the horizontal bars was, however, observed for the high Si alloy both at room temperature and 1500ºF. For the low Si LB-PBF alloy the decrease in ductility was observed only at 1500ºF. The lower ductility perpendicular to the build direction for the high Si alloy was attributed to the presence of cracks aligned along the build direction (Figure 9f).

For the high Si EB-PBF alloy, the effects of HIP'ing and specimen orientation on the mechanical properties of 0.080 inch (2mm) thick dog-bone tensile specimens are shown in Figure 15. A significant decrease of the UTS and ductility was observed for the specimens machined perpendicular to the build direction compared to the specimens machined along the build direction, which is again attributed to the preferential orientation of cracks along the build direction. HIP'ing had no effect on the tensile properties along the build direction of the high Si EB-PBF alloy, but resulted in a significant improvement of the UTS and ductility perpendicular to the build direction leading to relatively isotropic tensile properties for the HIP'ed material. These results are consistent with the crack removal observed after HIP'ing (Figure 12).

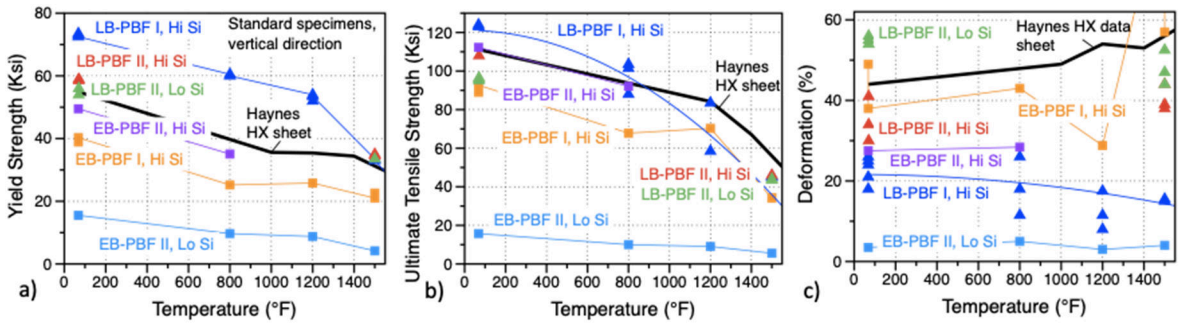

Figure 13: Comparison of the tensile properties between LB-PBF and EB-PBF alloys with low and high Si content, a) Yield strength, b) UTS and c) elongation at rupture

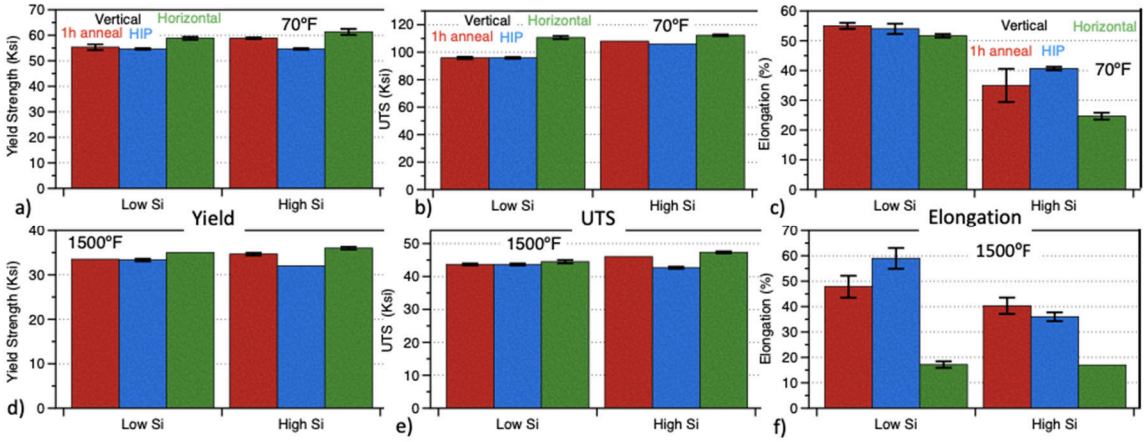

Figure 14: Comparison of the tensile properties of LB-PBF alloys along and perpendicular to the build direction, a) YS at 70ºF, b) UTS at 70ºF, c) Elongation at rupture at 1500ºF, d) YS at 1500ºF, e) UTS at 1500ºF, f) Elongation at rupture at 1500ºF

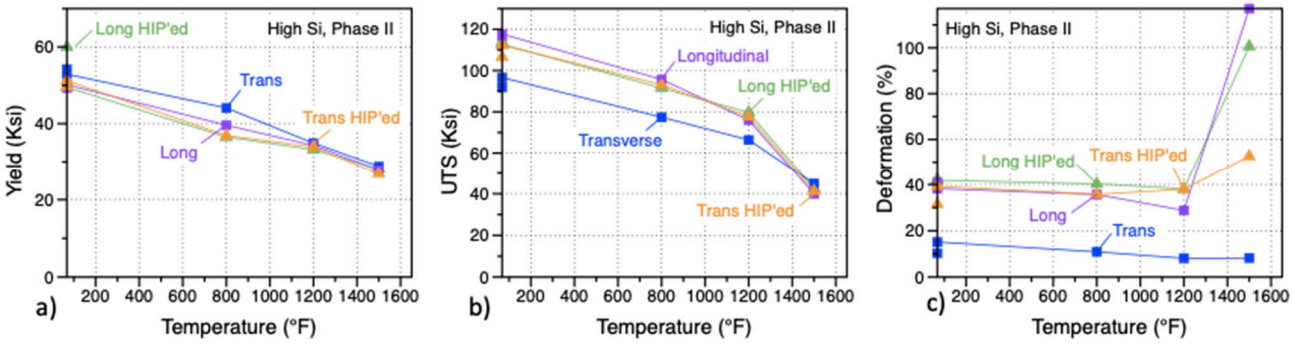

Figure 15: Tensile properties of dog-bone EB-PBF specimens along and perpendicular to the build direction in the as-fabricated and HIP'ed conditions, a) Yield strength, b) UTS and c) elongation at rupture

Fatigue Properties: A summary of the fatigue tests conducted on the LB-PBF and EB-PBF HX alloys is shown in Figure 16a and b, respectively. Fatigue tests on the LB-PBF were conducted at 1000ºF with a total strain of 0.6% on high Si and low Si alloys while the tests on the EB-PBF alloys were conducted at 800ºF with a 0.8% total deformation on the high Si alloy only. Due to the very low tensile properties of the low Si alloy, fatigue tests were not performed on this material. The low Si LB-PBF alloy exhibited better fatigue performance, with a significant increase of the number of cycles to failure (Nf) for both LB-PBF alloys after HIP'ing. Fracture surface analysis revealed a switch from crack initiation at defects inside the specimen after annealing to crack initiation at an oxide inclusion or at the specimen surfaces after HIP'ing (Figure 17). A decrease of Nf by a factor of two was observed for both alloys with annealed specimens machined perpendicular to the build direction.

Even after HIP'ing, the Nf values for the high Si phase II EB-PBF specimens were still lower than the Nf values measured for the as-fabricated high Si phase I EB-PBF. As expected, very early failures were observed for the specimens machined perpendicular to the build direction, again because of the presence of elongated cracks along the build direction.

These results highlight the drastic impact of the AM process type, build parameters, specimen orientation, and heat treatment on the microstructure and properties of Nickel Alloy X fabricated by AM processes.

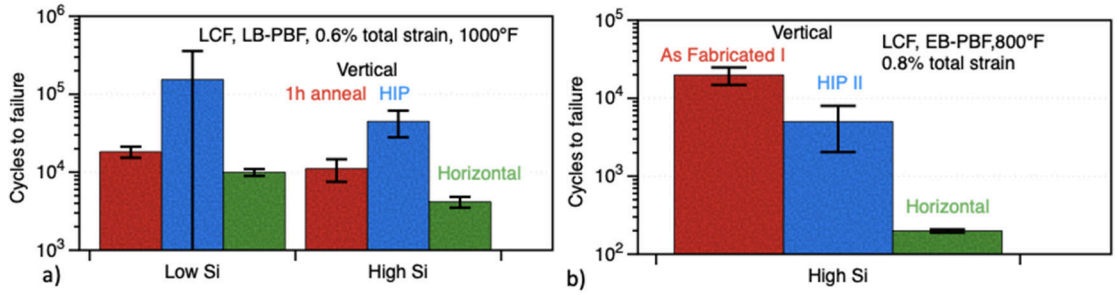

Figure 16: Number of cycles to failure, a) LB-PBF specimens tested at 1000ºF with a total strain of 0.6%, b) EB-PBF specimens tested at 800ºF with a total strain of 0.8%

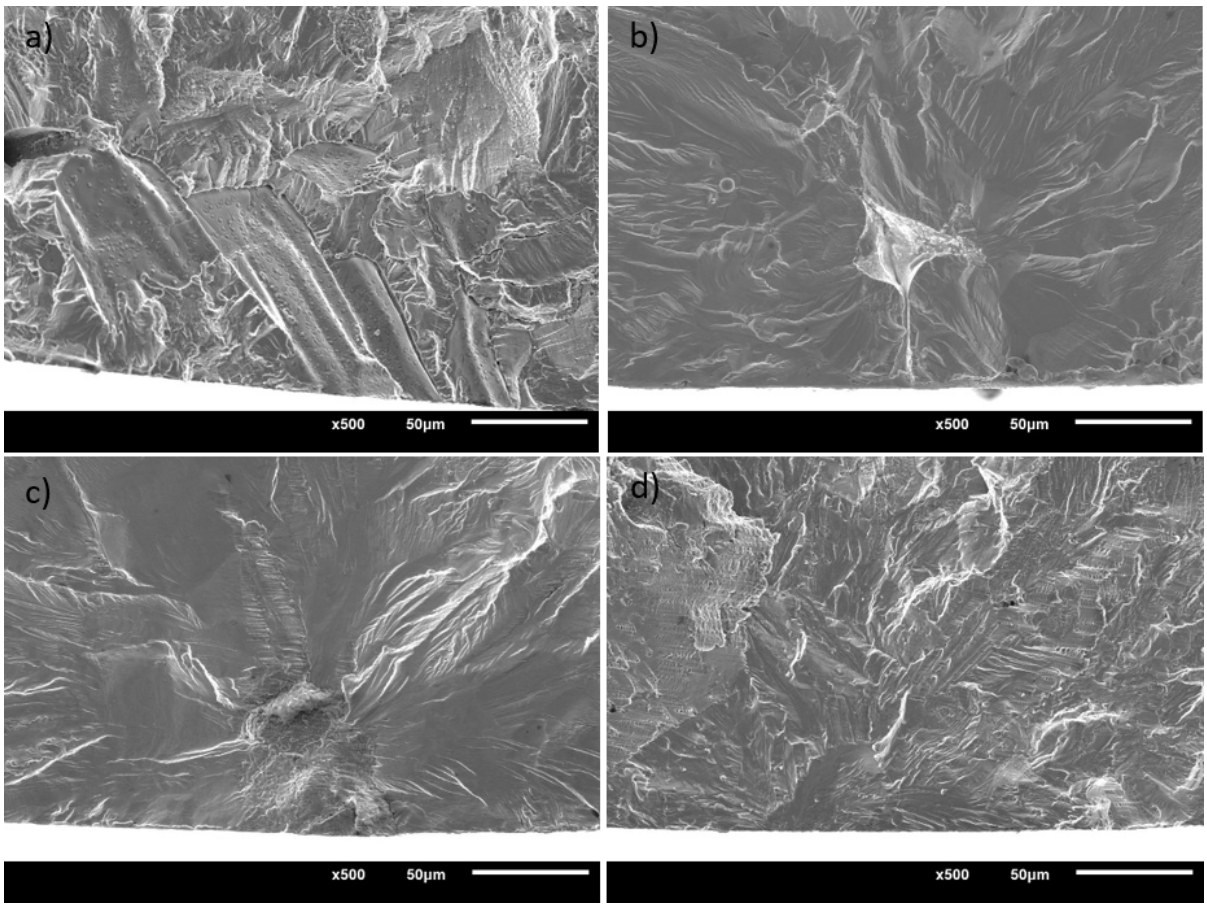

Figure 17: SEM images of the fracture initiation sites for LB-PBF LCF tests, a) "Vertical Annealed" High Si specimen, b) "Vertical Annealed" Low Si specimen, both showing irregular shaped discontinuities, c) "Vertical HIP'ed" low Si specimen and d) "Vertical HIP'ed" high Si specimen

1.2.5 Oxidation Properties (Precursor Powder Effect)

Oxidation testing was conducted at 1472°F (800ºC) in air on as-fabricated rectangular coupons ~0.4x0.8x0.06-0.08 inch in size. The LB-PBF oxidation coupons were fabricated along with the artifacts (Figure 4), while the EB-PBF coupons were machined from builds such as the one shown in Figure 18a. Half ring coupons ~0.080 inch (2mm) thick were also machined from cast Nickel Alloy X components to serve as a reference. The specimens were weighed every 100 hours and the specimen mass change curves are shown in Figure 18b. The EB-PBF coupons exhibited higher mass gains compared to the LB-PBF and cast Nickel Alloy X coupons. Spallation appeared to be minimum for all the specimens tested up to 2,000h. For both the LB- and EB-PDF alloys, increasing the Si content of the powder led to faster oxidation rates, particularly in the first 500 hours of testing. Coupons were interrupted after 1,100 hours of testing for microstructure characterization, and the coupon cross-sections are shown in Figure 19. The very rough surface finish of the EB-PBF coupons compared to the LB-PBF coupons is obvious in Figure 19a-d. A very convoluted interface was, indeed, observed for the EB-PBF coupons, with a larger convolution amplitude for the EB-PBF low Si. The high surface roughness for the EB-PBF specimens led to a higher surface in contact with the environment which certainly contributed to the higher specimen mass changes. In addition, Figure 19e-k show that the

oxide scale at the surface of the EB-PBF coupons was thicker compared to the scale at the surface of the LB-PBF or cast Nickel Alloy X coupons. The thickness of the scale on the cast coupons varied from one location to another. Many small voids were also observed beneath the oxide scale for the EB-PBF alloys, but only a few of these voids were observed for the LB-PBF and cast Nickel Alloy X coupons.

Finally, chemical maps for the high Si and low Si EB-PBF coupons exposed for 1100 hours at 1472°F (800ºC) are shown in Figure 20. For the high Si alloy, significant segregation of Si was observed at the alloy/scale interface with the formation of SiO_2 precipitates, while the high Mn content resulted in the formation of an outer Mn-rich scale. It is also worth noting that Mo-rich precipitates formed in the low Si alloy during exposure at 1472°F (800ºC).

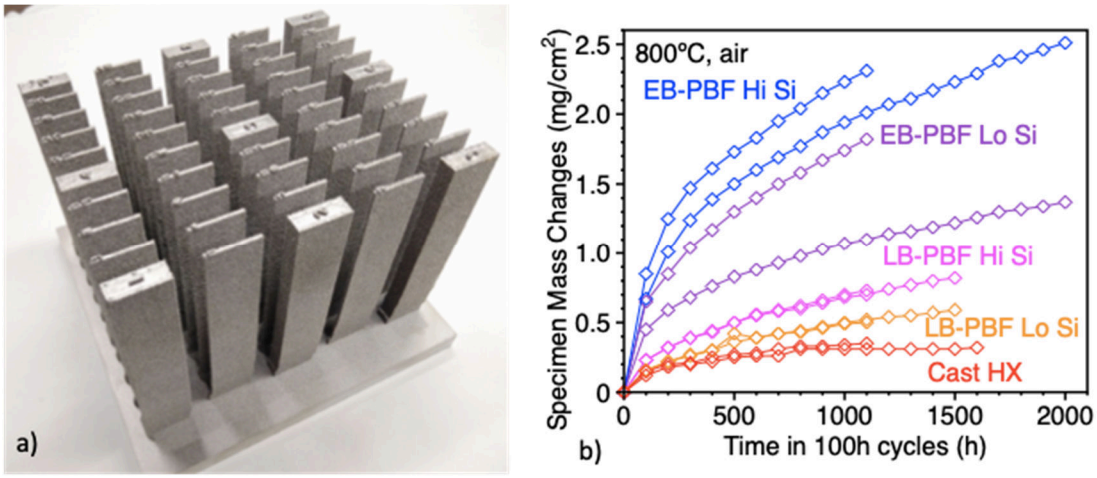

Figure 18: a) Thin-walled EB-PBF plates and b) Specimen mass changes of high Si and low Si LB-PBF and EB-PBF coupons for specimens exposed in air at 1472°F (800ºC) for up to 2,000h

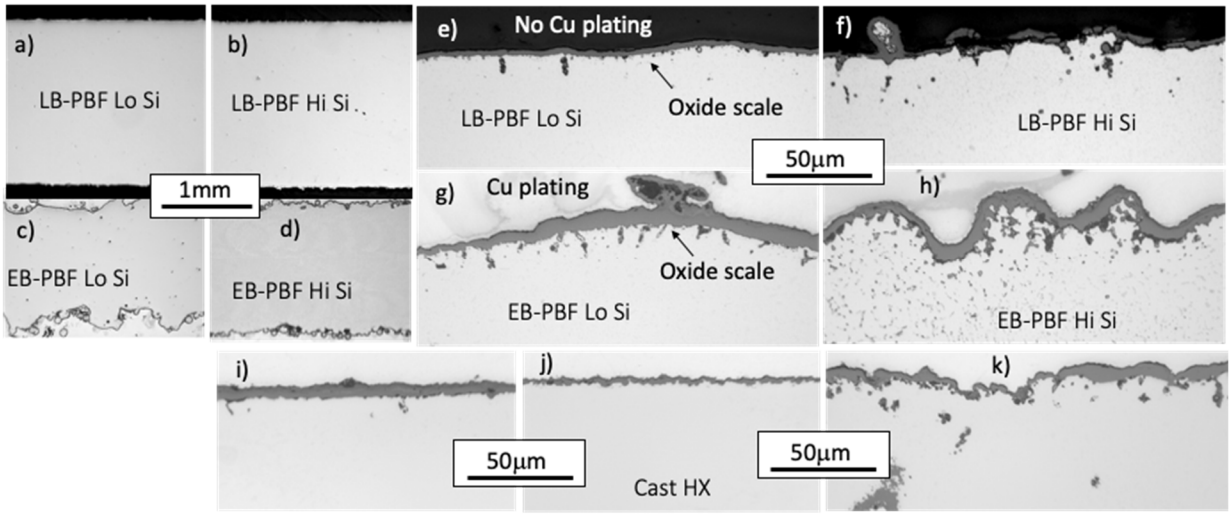

Figure 19: Optical cross-section micrographs of oxidation coupons exposed for 1100h at 1472°F (800ºC), a) and e) LB-PBF low Si, b) and f) LB-PBF High Si, c) and g) EB-PBF low Si, d) and h) EB-PBF High Si, i) to k) Cast Nickel Alloy X

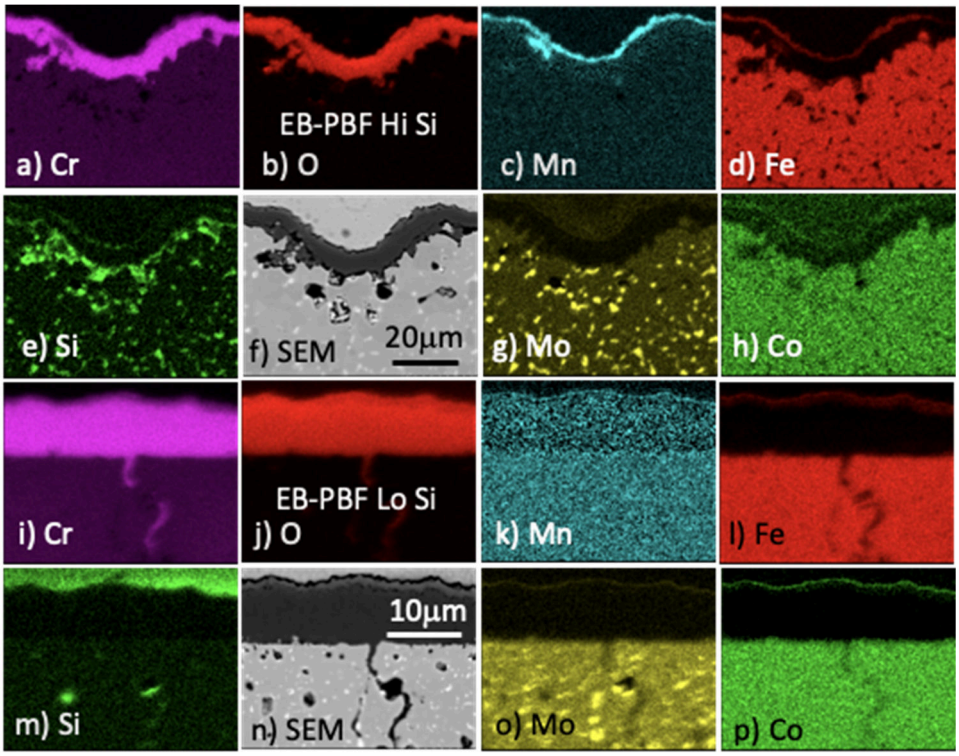

Figure 20: Chemical maps of the oxide scale formed at the surface of the EB-PBF alloys tested for 1100h at 1472°F (800ºC) in air, a)-h) High si alloy, i)-p) low Si alloy

1.3 IMPACTS

Prior phase I assessment of AM Nickel Alloy X (Ni-22Cr-18Fe-9Mo) material revealed substantial overlap of mechanical properties with those of conventional cast and wrought forms currently used in gas turbine applications. These preliminary results indicated the subject AM material was a viable alternative for manufacture of select turbine components; however, to move AM from the low volume development paradigm to a high-volume component production manufacturing mode, additional evaluation of AM process variability was needed.

Geometry impact: The LB-PBF process displayed acceptable feature resolution and surface roughness characteristics and has been identified as an appropriate metal AM process for components with fine detail requirements. However, feature resolution and surface roughness of the EB-PBF process were not suited for intricate geometries needed for turbine engine fuel injector components typically manufactured from Nickel Alloy X material. Despite the higher material throughput capability of the EB-PBF process, additional process development would be needed to improve the EB-PBF geometric capability prior to selection for widespread production of injector components. Alternately, future exploration of AM processes, such as binder jet, may provide both the desired feature resolution and high material throughput capability.

Chemistry impact: The composition of the precursor powder had an unanticipated effect on the AM material quality and associated mechanical properties. Even though the powder chemistries were held within the bounds of conventional material specification limits (Si concentration <1%), extensive cracking occurred in more than half of the builds with the subject powders evaluated. It is also worth noting that opposite trends were observed for the LB-PBF and EB-PBF processes, with high cracking frequency being observed for the high Si LB-PBF and low Si EB-PBF alloys.

The resultant reduction in fatigue life and tensile ductility would likely impact component durability of some turbine components. The sensitivity of AM Nickel Alloy X material properties to these apparently minor chemistry changes is an issue that AM users should consider when incorporating AM processes into the supply chain strategy.

Heat treat impact: Hot Isostatic Pressing (HIP) has historically been used by turbine engine manufacturers for improving the fatigue life of conventional cast turbine components, and the subject phase II work demonstrated similar responsiveness of AM materials to HIP processing. In the case of the micro-crack prone AM Nickel Alloy X variant, the low cycle fatigue life was more than doubled by HIP processing. These results demonstrate that HIP can be an effective post processing option for AM Nickel Alloy X to mitigate the effect of sub-surface discontinuities. The combination of optimal alloy chemistry, plus HIP processing is likely to provide AM material with the maximum fatigue capability.

Oxidation impact: The EB-PBF alloys exhibited higher specimen mass changes compared to the LB-PBF alloys likely because of the EB-PBF specimen higher roughness, but all the AM Nickel Alloy X materials evaluated in phase II displayed oxidation behavior suitable for high temperature applications in a turbine engine. Accordingly, excessive oxidation of AM Nickel Alloy X is considered an area of low risk and the need for additional materials development in this area is limited.

Through the subject phase II work, insights were gained into AM process type limitations and the effects of precursor powder and post-printing heat treatment on AM material behavior. These results have contributed to the body of knowledge needed to support component production implementation of AM processes at an industrial gas turbine engine equipment manufacturer. Trade-offs between the various processing options were quantified so that AM user can select the appropriate manufacturing path to meet specific component design and cost constraints. Additionally, these data support creation of material properties design curves for mechanical analysis of turbine part durability. The processing information generated will be incorporated into manufacturing controls that ensure production of consistent material quality.

1.4 CONCLUSIONS

Extensive characterization of AM Nickel Alloy X (Ni-22Cr-18Fe-9Mo) artifacts fabricated by LB-PBF and EB-PBF using powders with low Si and high Si content revealed the need to control the alloy chemistry to avoid significant cracking. The combination of optimal alloy chemistry plus HIP processing will yield the best fatigue performance for AM Nickel Alloy X components. The oxidation rates for all the AM Nickel Alloy X materials were found acceptable for gas turbine applications. Feature resolution and surface roughness for the LB-PBF process is suited for intricate geometries needed for turbine engine fuel injector components. This is not the case for the EB-PBF process, and additional process development would be required to improve the EB-PBF system geometric capability and take advantage of the higher EB-PBF throughput.

References

[1] S. Dryepondt, M. Kirka, B.A. Pint and D. Ryan, “Comparison of Electron Beam and Laser Beam Powder Bed Fusion Additive”, ORNL report, ORNL/TM-2016/47 (2016).
[2] D. Tomus, T. Jarvis, X. Wu, J. Mei, P. Rometsch, E. Henry, J-F Rideau and S. Vaillant, “Controlling the microstructure of Hastelloy-X components manufactured by selective laser melting”, Physics Procedia, 41, 823-827 (2013).
[3] Haynes International’s datasheet, Hastelloy X alloy, Brochure H-3009, https://www.haynesintl.com/docs/default-source/pdfs/new-alloy-brochures/high-temperature-alloys/brochures/x-brochure.pdf

2. PARTNER BACKGROUND

Solar Turbines Incorporated, a wholly owned subsidiary of Caterpillar since 1981, headquartered in San Diego, California, employs approximately 8,000 employees, many of which are located at the headquarters in San Diego, California. Solar Turbines is a leading industrial gas turbine OEM, offering a range of gas turbines and turbomachinery equipment in the 1- 23 MW range for oil & gas exploration and transmission, and for power generation and cogeneration. Solar Turbines' state-of-the-art gas turbines are complemented by a line of compressors that can be matched with Solar Turbines equipment, or that of other OEMs. Over 15,000 gas turbines units and over 6,000 gas compressors, sold in over 100 countries, account for more than 2.7 billion fleet operating hours.

Solar Turbines has over 50 years of experience with the design, development and commercialization of industrial gas turbines and turbomachinery products. Solar Turbines has a long record of development of gas turbine technologies from internally funded and government programs. An example of a successful government-industry partnership was the DOE-Solar Advanced Turbine Systems (ATS) program, which resulted in the development of the 4.6 MWe Mercury 50 recuperated gas turbine. Solar Turbines has also been involved in the development of gas turbine products for renewable energy including bio-gas and solar energy.